THE ASTROPHYSICAL JOURNAL, 286:186–195, 1984 November 1

X-RAY MEASUREMENTS OF THE NONSPHERICAL MASS DISTRIBUTION IN THE CLUSTER OF GALAXIES A2256

D. FABRICANT, G. RYBICKI, AND P. GORENSTEIN
Harvard-Smithsonian Center for Astrophysics
Received 1984 March 26; accepted 1984 May 18

ABSTRACT

We describe a technique for the analysis of X-ray surface brightness maps of rich clusters of galaxies with a smooth X-ray morphology and appropriate bilateral symmetry to yield an accurate estimate of the underlying cluster mass distribution. This method assumes that the X-ray emitting gas is in hydrostatic equilibrium in the gravitational potential of the cluster, and that the cluster possesses an axis of symmetry that lies in the plane of the sky. The errors associated with the latter assumption are discussed. We apply this technique to the cluster of galaxies A2256 and find that the mass distribution departs significantly from spherical symmetry, with axial ratios of approximately 1.6. This is to be compared with the axial ratio of 2–3.3 found for the galaxy distribution. We find that the surfaces of constant total density are more complex than similar oblate or prolate spheroids with a fixed center. The radially integrated mass derived from the X-ray data is consistent with that estimated from the galaxy surface density and velocity dispersion.

Subject headings: galaxies: clustering — X-rays: sources

I. INTRODUCTION

The subject of this paper is the detailed description of the mass distribution in the rich cluster of galaxies A2256. The starting point of the analysis is a map of X-ray surface brightness, obtained with the imaging proportional counter (IPC) aboard the *Einstein Observatory*, rather than the more familiar chart of galaxy positions within the cluster. Because the X-ray emission is thermal, arising from a pervasive hot gas thought to be in hydrostatic equilibrium in the gravitational potential of the cluster, the surface brightness data and X-ray spectral measurements can be analyzed to yield that potential. In particular, the X-ray data allow a sensitive search for departures from spherical symmetry. The surface brightness map of A2256 shows a pronounced ellipticity, indicating that the underlying mass distribution is flattened.

Departures from spherical symmetry have been recognized increasingly as an important feature of clusters, one that might be related to formation mechanisms. There are at present few detailed predictions for the geometry and axial ratios to be expected from the competing theories of the formation of clusters and other large-scale structures, but this situation might be expected to change in the next few years. Recently, observational evidence based on optical galaxy counts has been presented indicating that clusters are in general rather elongated, with typical axial ratios of 2 (Binggeli 1982; Carter and Metcalfe 1980). However, the interpretation of these data is complicated by the fact that most of the matter in clusters is nonluminous, and the galaxies may or may not have the same distribution as the dark matter. The action of dynamical friction (Binney 1977; Merritt 1983) may tend to produce a galaxy distribution that is more flattened and centrally peaked than that of the dark matter. X-ray observations provide an excellent means of studying this problem, because the X-ray emitting gas does not discriminate between luminous and nonluminous matter. Furthermore, the X-ray observations do not suffer from the small-number statistics typical of many of the existing optical studies.

Most previous analyses of cluster X-ray emission have treated gas with an assumed polytropic equation of state in hydrostatic equilibrium in a spherically symmetric potential. Several approaches are reviewed by Cavaliere (1980). We wish to relax the constraint of spherical symmetry to consider clusters with a single axis of symmetry. Binney and Strimpel (1978) and Strimpel and Binney (1979) have treated the related problem of estimating spheroidal cluster potentials from galaxy counts and have produced predicted X-ray surface brightness maps for the Coma Cluster. Hirayama and Ikeuchi (1978) considered ellipsoidal models for the mass distribution in the Perseus Cluster in response to reports that the X-ray emission was highly nonspherical. However, our data on A2256 show obvious deviations from the simple ellipsoidal models, and we have attempted to derive the mass distribution from the X-ray observations directly. Our approach is to deproject the observed surface brightness distribution to yield the volume emissivity, assuming an axis of symmetry perpendicular to the line of sight. Assuming that the gas is in hydrostatic equilibrium and using our knowledge of the gas temperature (and its gradient), we may derive the mass distribution in the cluster.

II. OBSERVATIONS AND PRELIMINARY ANALYSIS

a) Surface Brightness Map

A2256 was chosen for study because it has an X-ray morphology and optical characteristics similar to the Coma Cluster but is at an optimum distance ($z = 0.059$; Faber and Dressler 1977) for the format of the IPC on the *Einstein Observatory*. The cluster is large enough to provide many pixels of angular resolution, yet small enough so that a few pointings include sufficient coverage of off-cluster regions, allowing simultaneous background measurement. The data described here were obtained in five pointings of the IPC. One pointing was centered near A2256, while the others were offset to the north, south, east, and west by 25′. The observations are shown schematically in Figure 1, and the observation dates, pointing directions, and effective exposure times are summarized in Table 1.

In order to produce a map of the X-ray surface brightness, it

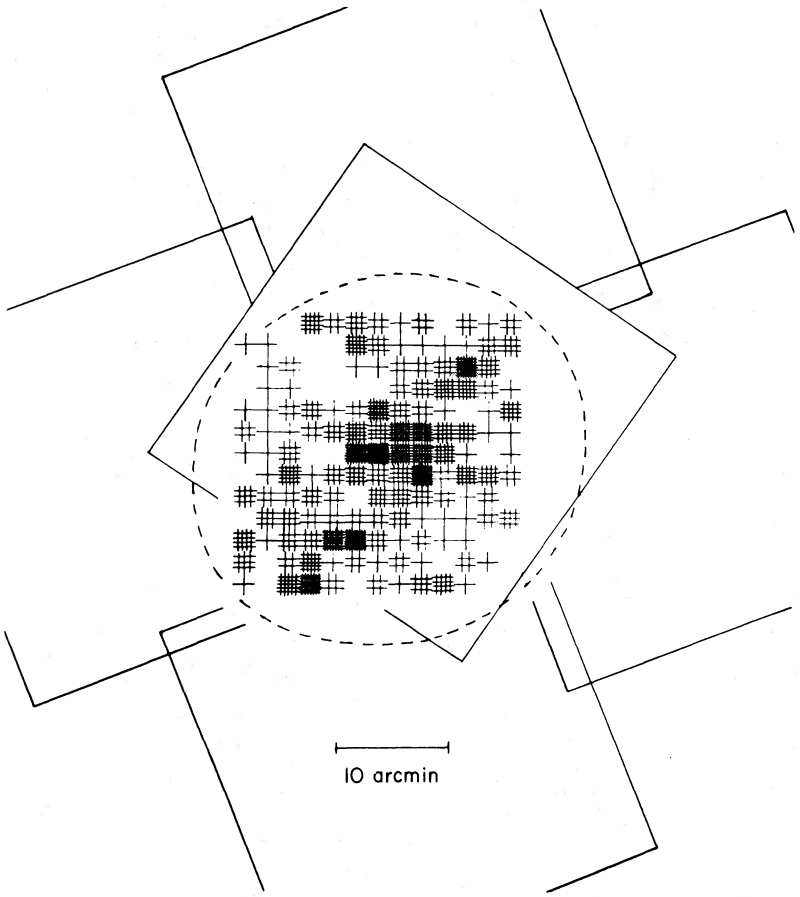

FIG. 1.—A schematic representation of the IPC fields used to study the X-ray emission from A2256, superposed on a plot of the surface density of galaxies in the cluster center. The galaxy counts (for a region 25′ square) are complete to $M_F = 18.5$ and are taken from Dressler (1976). One vertical and one horizontal bar are plotted for each galaxy within a 2′ square bin. The dotted line shows the approximate extent of the outermost isophote used in the following analysis.

is necessary to merge the raw data from these observations, subtract background, and correct for exposure variations due to telescope vignetting and overlapping fields. The routine *Einstein* data processing system removes spacecraft motion and corrects for nonlinearities in the spatial response of the detector and for gain variations over time and with position in the detector. In order to eliminate background variations caused by solar X-rays scattered by the atmosphere, data acquired during sunlit portions of the orbit were rejected whenever the telescope pointed within 52° of the Earth's limb. The data from each field were binned in a common 64 × 64-element array with a cell size of 1.′6 on a side. Data from those pulse-height channels resulting in the best signal-to-noise ratio were used, corresponding to X-ray energies between 0.3 and 3.5 keV. Only the data from the central 34′ × 34′ of the detector were used to minimize any errors resulting from imperfect vignetting correction. Even with this truncation, the composite map from the five fields gives complete coverage to a radial distance of 28′ from the cluster center, corresponding to a radius of 2.8 Mpc. We use a Hubble constant of 50 km s^{-1} Mpc^{-1} throughout this paper, which results in a convenient approximate scale of 100 kpc $arcmin^{-1}$ at the redshift of A2256.

TABLE 1

Einstein OBSERVATIONS OF A2256

Einstein Sequence No.	Date Observed	Pointing Direction (Field Center)	Effective Exposure Time (s)
300.....	1979 Apr 10, 11	$17^h\ 6^m30^s$; 78°47′	7054
7527.....	1980 Feb 15–17	17 15 15 ; 78 42	11744
7528.....	1980 Feb 13–16	16 58 14 ; 78 42	10161
7529.....	1980 Feb 13–16	17 6 45 ; 78 17	8167
7530.....	1980 Feb 13–15	17 6 45 ; 79 7	14308

In order to estimate the total X-ray plus non–X-ray background, data from five high-galactic-latitude deep surveys with similar data-screening constraints were binned together in constant detector coordinates. This background map was then normalized appropriately and placed in a 64 × 64 array at the position of each of the five A2256 fields. With the chosen binning, each element of the background map for an individual field contained an average of 60 counts prior to normalization. The normalized background array could then be subtracted directly from the data array to correct for background. The residual surface brightness at radii more than 35′ from the cluster center was studied as a function of the normalization of the background array. It was found that a normalization factor of 1.19 times the ratio of the exposure times resulted in a residual closest to zero, and this factor was adopted. Variations in background of this magnitude from field to field are not uncommon. Because the lowest surface brightness level (approximately 10 counts per cell after background subtraction) used in the subsequent analysis was twice the background level, a 10% error in normalization would result in a 5% surface-brightness error. The background-subtracted

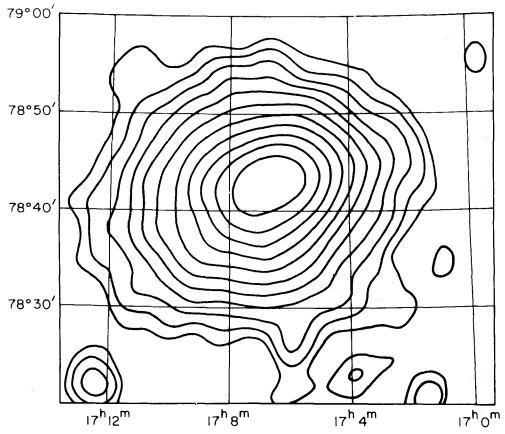

FIG. 2

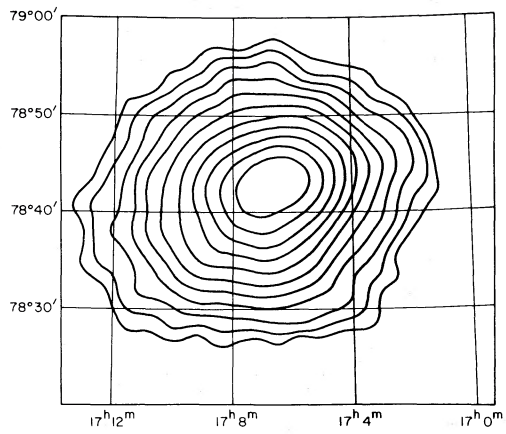

FIG. 3

FIG. 2.—A 0.3–3.5 keV contour map of the X-ray surface brightness of A2256. The X-ray surface brightness peaks at R.A. $17^h6^m48^s$, decl. 78°43′. Background has been subtracted, and the map has been corrected for exposure. The contour levels are separated by a factor of 1.5 in surface brightness. The highest level shown corresponds to 9.4×10^{-3} counts s^{-1} arcmin^{-2} or 2.7×10^{-13} ergs cm^{-2} s^{-1} arcmin^{-2} in the 0.3–3.5 keV band. The scale is 100 kpc arcmin^{-1} for $H_0 = 50$ km s^{-1} Mpc^{-1}. The resolution of this map is 3′.5 FWHM.

FIG. 3.—Same as Fig. 2, except that unresolved sources have been subtracted. None of these sources is associated with a cluster galaxy.

array, once corrected for exposure, yields a surface brightness map ready for subsequent analysis. As a final step, the map was rebinned in 0′.27 cells and smoothed by convolution with a Gaussian function of 3′.2 FWHM to minimize the visual effect of the large bins necessitated by the background subtraction. The resultant map is shown in Figure 2. The effective resolution of this map is 3′.5 FWHM, when the 1′.5 FWHM detector resolution is added in quadrature. Figure 3 is the same map but with three unresolved sources within the lowest cluster contour subtracted. Sources outside the lowest cluster contour were suppressed. None of these sources is identified with a galaxy in the cluster.

As can be seen in Figure 3, the isophotes are not circular. We have quantified the ellipticity of each of the 11 isophotes in Figure 3, which are separated by a factor of 1.5 in surface brightness. The two principal moments of inertia about the center of mass of the plane surface bounded by each isophote were calculated. Using the fact that the moments of inertia of a plane elliptical surface (semimajor radius a, semiminor radius b) are $\pi ab^4/4$ and $\pi a^3 b/4$ about the major and minor axes, respectively, the axial ratios may be calculated. Table 2 summarizes the center-of-mass positions, the axial ratios, and the position angle of the major axes for each isophote.

It is apparent from examining Table 2 that the center-of-mass position is not constant for the isophotes, and in fact moves by approximately 2′ to the southeast from the highest to the lowest isophote. This motion is predominantly along the major axis, as may be verified from Figure 3. Two other features of note are the fact that the position angle of the principal axis is not strongly dependent on radius, and that the ellipticity of the isophotes decreases with radius. A twist in the position angle of the isophotes is usually interpreted as a sign of triaxiality, but there is no convincing evidence for this effect in our data. The decreasing ellipticity of the isophotes with radius is expected, since the potential set up by any self-gravitating ellipsoidal mass distribution becomes more spherical with

TABLE 2

RESULTS OF ELLIPTICAL ANALYSIS OF X-RAY SURFACE BRIGHTNESS DATA

Average Radius (arcmin)	Axial Ratio	Isophote Major-Axis Position Angle North to East	Radial Movement of Isophote Center (arcmin)	Angle between Major Axis and Vector of Center Movement
3.26.....	1.38	120.09	0	...
4.69.....	1.30	120.38	0.26	29.9
5.91.....	1.25	120.24	0.43	32.0
7.11.....	1.23	122.30	0.64	20.8
8.40.....	1.23	124.47	0.98	10.1
9.70.....	1.21	123.06	1.27	6.1
10.96.....	1.18	120.44	1.37	4.9
12.23.....	1.15	119.31	1.40	7.6
13.71.....	1.13	117.53	1.54	15.8
15.18.....	1.17	113.38	1.92	16.8
16.45.....	1.16	112.45	2.02	16.7

NOTE.—The analyzed isophotes are separated by a factor of 1.5 in surface brightness and are the same as those plotted in the contour maps. The highest level corresponds to a flux of 2.7×10^{-13} ergs cm^{-2} s^{-1} arcmin^{-2} in the 0.3–3.5 keV band.

increasing radius. Because the movement of the isophote centers follows the major axis, and the position angle of the isophotes is relatively constant, the surface brightness distribution retains a bilateral symmetry, a fact we exploit in the following deprojection.

b) *Spectral Fits*

Low-resolution spectral data are available from the IPC. These have been binned in three annuli with radii of 0′–5′, 5′–10′, and 10′–15′. These data, after subtraction of background estimated from a high-galactic-latitude deep survey at the same detector gain, were fitted with thermal models of Raymond and Smith (1981, private communication) with interstellar absorption. Due to the limited bandwidth of the *Einstein* mirror and the modest spectral resolution of the IPC, coupled with the high temperature of the cluster gas, we are able to derive only lower limits on the gas temperature, which become less stringent with decreasing surface brightness. Limiting the maximum allowed interstellar hydrogen column to three times the 21 cm value of 6×10^{20} cm^{-2}, we obtain 90% confidence limits of greater than 5.2 keV (0′–5′), greater than 4.4 keV (5′–10′), and greater than 3.5 keV (10′–15′). These measurements are consistent with those obtained from nonimaging instruments with a large field of view, of 7.7 ± 1.0 keV (Mitchell *et al.* 1979) and 7.0(+3.0, −2.0) keV (Mushotzky *et al.* 1978). We adopt a temperature of 8 keV for the purposes of the following analysis.

III. DETERMINATION OF THE CLUSTER MASS DISTRIBUTION

a) *Technique*

There are three principal steps in the analysis of the X-ray data to yield the cluster mass distribution: (1) the deprojection of the X-ray surface brightness to give the volume X-ray emissivity of the hot gas, (2) the determination of the gas density distribution from the emissivity using what is known about the gas temperature profile, and (3) the application of Poisson's equation to relate the total density distribution to the gas density and temperature.

The first step is in practice the most difficult and uncertain in this analysis. It is in principle impossible to deduce a general emissivity distribution from a single projection unless further assumptions are made. In our case, the bilateral symmetry of the surface brightness map suggests that the underlying emissivity distribution is axisymmetric, the axis of symmetry being projected into the major axis of our map. Although this seems to be a reasonable assumption, we recognize that the apparent bilateral symmetry may be an accident of projection with hidden elongations or contractions along the line of sight. We further assume that the axis of symmetry lies in the plane of the sky; this corresponds to the assumption that the inclination angle i, measured from the line of sight, is 90°. We are forced to make this assumption, because otherwise the deprojection problem cannot be solved uniquely (see Rybicki 1984). However, it is possible to estimate the errors associated with this assumption, and we do so in § IIIc. The assumptions we describe here are essentially the same as those used by Binney and Strimpel (1978).

The actual deprojection (step 1) was performed using a standard Abel integral, after some unsatisfactory experimentation with Hankel transforms on Fourier transformed data. The volume emissivity $\epsilon(r, x)$, in cylindrical coordinates, is related to the surface brightness $I(x, y)$, in Cartesian coordinates, by

$$\epsilon(r, x) = -\frac{1}{\pi} \int_r^\infty \frac{\partial I/\partial y}{(y^2 - r^2)^{1/2}}\, dy \,, \tag{1}$$

where the x-axis is the symmetry axis. Errors in the numerical calculation of the Abel integral were minimized by interpolating between the tabulated surface brightness entries with a spline function, which was then inverted analytically.

We carry out step 2 by noting that if the gas is isothermal, its density is proportional to the square root of the emissivity. This relation is not exactly correct for nonisothermal gas, but because the change in emissivity in the *Einstein* IPC bandpass with temperature is small (e.g., Fabricant, Lecar, and Gorenstein 1980), it remains a good approximation.

To proceed with step 3, we assume that the gas is nonrotating and in hydrostatic equilibrium, which implies

$$\frac{1}{\rho_g} \nabla p_g = -\nabla \Phi \,, \tag{2}$$

where ρ_g and p_g are the gas density and pressure, respectively. The gravitational potential Φ is related to the total density by Poisson's equation:

$$\nabla^2 \Phi = 4\pi G \rho_{\text{total}} \,, \tag{3}$$

where ρ_{total} is the total mass density and G is the gravitational constant. Combining equations (2) and (3), we have

$$\rho_{\text{total}} = -\frac{1}{4\pi G} \nabla \cdot \left[\frac{1}{\rho_g} \nabla p_g \right] . \tag{4}$$

This equation allows one to determine the total mass density within the cluster (including optically dark matter) from properties of the gas alone.

Since the pressure of the gas is not directly measurable, we introduce the equation of state of the gas:

$$p_g = \frac{\rho_g k T_g}{\mu M_p} \,, \tag{5}$$

where k is Boltzmann's constant, M_p is the proton mass, T_g is the gas temperature, and μ is the mean molecular weight of the gas, assumed constant. If the gas is isothermal, then equation (4) can be written

$$\rho_{\text{total}} = -\frac{k T_g}{4\pi G \mu M_p} \nabla^2 \ln \rho_g \,. \tag{6}$$

On the other hand, if the gas obeys a polytropic law of the form $p_g \propto \rho_g^\gamma$ where γ is a constant (the polytropic exponent), then it follows that

$$\rho_{\text{total}} = -\frac{\gamma k T_g(0)}{4\pi G(\gamma - 1)\mu M_p} \nabla^2 \left[\frac{\rho_g(r)}{\rho_g(0)} \right]^{\gamma - 1} . \tag{7}$$

The deprojection method discussed above requires that the surface brightness distribution have at least one axis of symmetry, which we assume to lie in the plane of the sky. In order to minimize the effect of statistical fluctuations in our data, we have chosen to deproject an idealized surface brightness map in which the isophotes are perfect ellipses with the attributes presented in Table 2. Because the single observed axis of symmetry lies along the major axis of the surface brightness distribution, only a prolate deprojection is formally possible. In

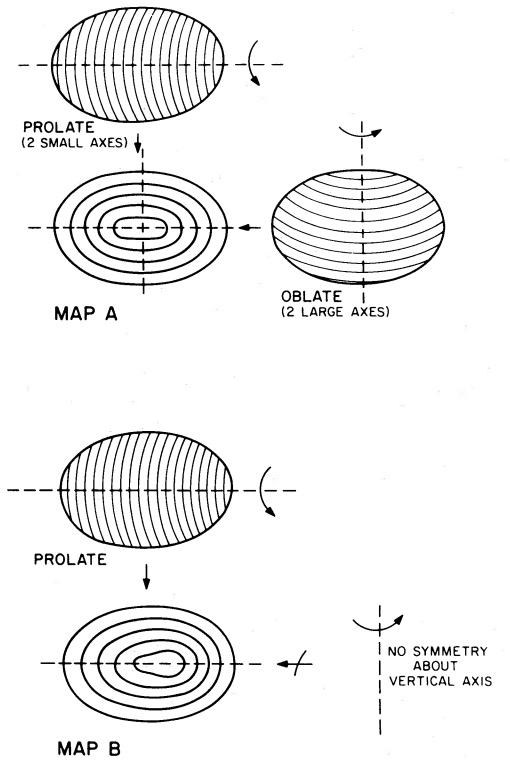

FIG. 4.—This figure illustrates the fact that a surface brightness map with bilateral symmetry about two axes (*Map A*) may be produced by an emissivity distribution with rotational symmetry about either of these axes. If it has bilateral symmetry about a single axis (*Map B*), one type of rotational symmetry is excluded. However, even if rotational symmetry is allowed, less symmetric emissivity distributions are possible (see text).

order to allow both oblate and prolate deprojections, two idealized maps were created. One models fairly realistically the movement of the isophote centers (assuming all movement along the major axis), while the other ignores this feature of the data. The map with two axis of symmetry can be deprojected assuming either an oblate or a prolate geometry, and the error caused by neglecting the movement of the isophote centers can be assessed by comparing the prolate deprojection with that from the more realistic map. Figure 4 illustrates the relationship between the symmetries of the surface brightness map and possible emissivity distributions. The maps were numerically calculated by iteratively solving (using Newton's method) the equation of an ellipse with analytic fits relating the major axis to the minor axis, and the isophote center to the minor axis. Given the appropriate major and minor axes, the surface brightness was extracted from another analytic expression. The idealized surface brightness maps are shown in Figures 5 and 6.

b) Derived Total Density Maps

Figures 7, 8, and 9 are contour plots of the derived total density distribution based on the oblate and prolate deprojections of the idealized surface brightness shown in Figure 5, and a prolate deprojection of the surface brightness map shown in Figure 6, respectively. These total density maps are in cylindrical coordinates, and correspond to the density on a plane surface intersecting the symmetry axis of the cluster. As discussed above, these maps were derived under the assumption that the symmetry axis lies in the plane of the sky.

c) Correction for Inclination Angle Other than 90°

Although the deprojection for an arbitrary assumed inclination angle i between the line of sight and the axis of symmetry cannot be performed uniquely, we have estimated the effect of an angle other than 90°. The projected appearance of a distribution whose surfaces of constant emissivity are similar oblate or prolate spheroids can be analytically calculated as a function of i. We reintroduce Cartesian coordinates x and y in the plane of the sky such that the x-axis lies along the projection of the symmetry axis. The surface brightness distributions viewed at 90° inclination is related to that viewed at inclination i by the expression

$$I_{90}(x, y) = RI_i(Rx, y) , \tag{8}$$

where

$$R = \frac{\sin i}{[1 - (B/A)^2 \cos^2 i]^{1/2}} . \tag{9}$$

Here B/A is the axial ratio of the ellipses that appear in projection along the y- and x-axes. This ratio is greater than unity in

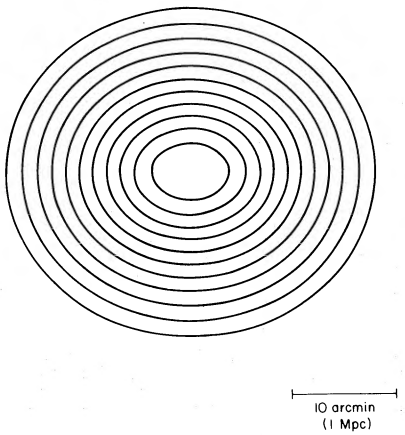

FIG. 5

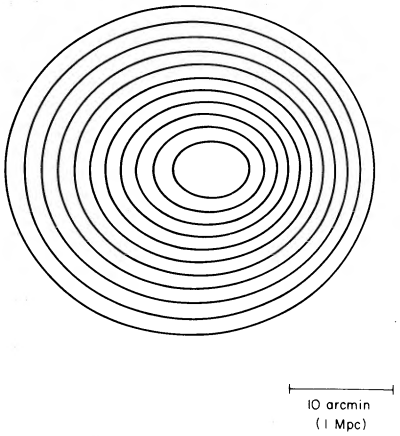

FIG. 6

FIG. 5.—An idealized representation of the X-ray surface brightness data in Fig. 3. The isophotes have been replaced with perfect ellipses with the same effective axial ratios as the actual data (see text). The contour levels are the same as those in Figs. 2 and 3.

FIG. 6.—Same as Fig. 5, except that the movement of the isophote centers with radius has been included.

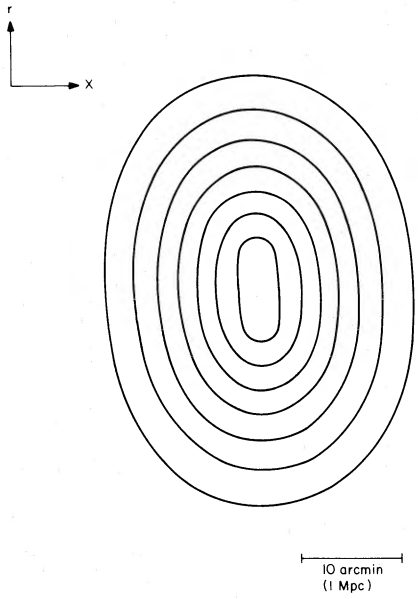

FIG. 7

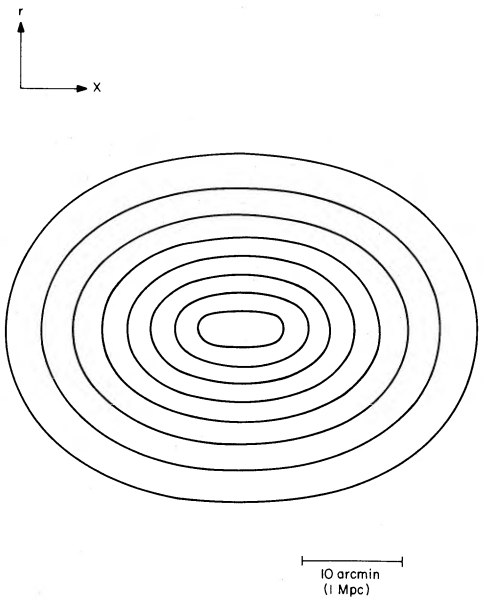

FIG. 8

FIG. 7.—A contour map of the derived total density distribution in A2256 assuming an oblate geometry and an isothermal X-ray emitting gas, and beginning with the idealized surface brightness map of Fig. 5. This map is plotted in cylindrical coordinates, and corresponds to the density on a plane surface intersecting the symmetry axis of the cluster (the x-axis). The contour levels are separated by a factor of 1.5 in total density, with the highest level at 1.5×10^{-26} g cm^{-3}.

FIG. 8.—Same as Fig. 7, except that a prolate geometry has been assumed. The top level corresponds to a density of 2.25×10^{-26} g cm^{-3}.

the oblate case and less than unity in the prolate case. The axial ratio of the emissivity distribution is related to the apparent axial ratio of the surface brightness distribution by

$$B_e/A_e = R(B/A) . \quad (10)$$

Equations (8)–(10) are derived in the Appendix.

Although the surfaces of constant emissivity are apparently not similar ellipsoids, we have calculated correction factors based on the average observed (surface brightness) axial ratio of 1.22 for inclination angles of 70° and 50°. These factors, applied to the observed axial ratios of the surface brightness, give an estimate of the surface brightness that would be observed at 90° inclination. This corrected surface brightness distribution could then be deprojected as described previously, and the standard analysis applied. Table 3 lists the axial ratios of the surfaces of constant total density at various fixed values of density for inclination angles of 90°, 70°, and 50°. Since we wished to include both oblate and prolate geometries, the axial ratios for these inclination angles are derived for the fixed-center surface brightness approximation plotted in Figure 4. However, for 90° inclination angle, the axial ratios for a fixed value of total density are very similar for the prolate deprojections with and without the fixed-center approximation.

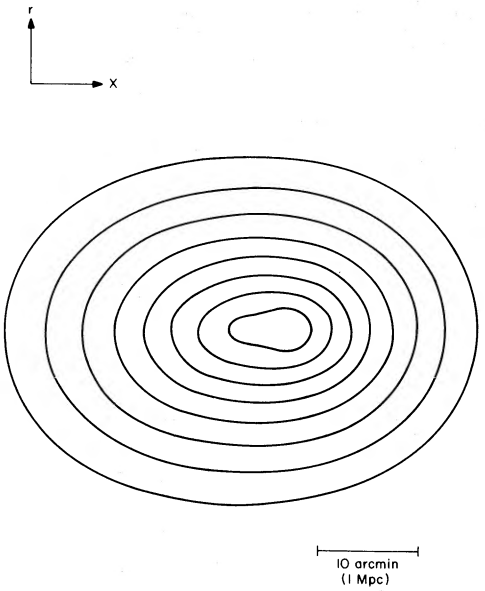

FIG. 9.—Same as Fig. 8, except that the idealized surface brightness map of Fig. 6 has been used as a starting point. The movement of the centers of the surfaces of constant density reflects the movement of the isophote centers, although the axial ratios are essentially unchanged from the map plotted in Fig. 8.

d) Effect of Extreme Temperature Gradients

In the previous analysis, we have assumed that the X-ray emitting gas is isothermal with a temperature of 8 keV, an assumption consistent with the available spectral data. However, these data are also consistent with a nonzero temperature gradient. In order to investigate how sensitive our results are to temperature gradients, we have used equation (5) to derive a total density distribution under the assumption that the gas is an adiabatic polytrope ($\gamma = 5/3$). Polytropic models have temperatures that decrease with radius. Since no sign of central gas cooling is observed in A2256, we have not considered positive temperature gradients (Jones and Forman 1984). We have taken the same gas density distribution used for the isothermal case, and calculated the radial surface brightness profile, emission-weighted temperature as a function of (projected) radius, and overall emission-weighted temperature for an adiabatic model using the thermal-emission

TABLE 3

AXIAL RATIOS FOR OBLATE AND PROLATE MODELS AS A FUNCTION OF INCLINATION ANGLE

OBLATE (FIXED ISOPHOTE CENTERS)			PROLATE (FIXED ISOPHOTE CENTERS)		
Density	Average Radius (arcmin)	Axial Ratio	Density	Average Radius (arcmin)	Axial Ratio
		Inclination Angle 90°			
66.7.....	5.7	1.80	100	4.9	1.79
44.4.....	7.8	1.64	66.7	7.0	1.62
29.6.....	9.9	1.57	44.4	9.0	1.53
19.8.....	12.3	1.52	29.6	11.3	1.48
13.2.....	15.0	1.48	19.8	13.8	1.44
8.8.....	18.1	1.42	13.2	16.7	1.39
			8.8	20.2	1.33
		Inclination Angle 70°			
66.7.....	5.7	1.88	100	4.9	1.85
44.4.....	7.8	1.73	66.7	7.0	1.67
29.6.....	9.8	1.67	44.4	9.1	1.59
19.8.....	12.1	1.63	29.6	11.4	1.54
13.2.....	14.8	1.60	19.8	13.9	1.50
8.8.....	17.8	1.55	13.2	16.9	1.45
			8.8	20.2	1.38
		Inclination Angle 50°			
100	4.1	2.67	100	5.0	2.09
66.7.....	5.9	2.39	66.7	7.1	1.89
44.4.....	7.7	2.33	44.4	9.3	1.81
29.6.....	9.5	2.34	29.6	11.7	1.76
19.8.....	11.5	2.37	19.8	14.3	1.73
13.2.....	13.6	2.43	13.2	17.3	1.70
8.8.....	15.9	2.40	8.8	20.8	1.64

NOTE.—Density is in units of 1.5×10^{-28} g cm^{-3} for $H_0 = 50$ km s^{-1} Mpc^{-1}.

models of Raymond and Smith (1981, private communication). In order to produce an emission-weighted temperature near the observed 8 keV, a central gas temperature of 16 keV is required. Although the surface brightness profile for an adiabatic model is expected to be steeper than that of an isothermal model for a fixed density distribution, the normalized surface brightness within a radius of 15′ agrees with the observed surface brightness to an accuracy better than 15%, which is acceptable for our purposes of error estimation. The emission-weighted temperature (integrated along the line of sight) as a function of radius is consistent with the IPC spectral data but follows the most extreme negative gradient allowed. The derived total mass distribution is much more centrally condensed for the adiabatic case, with a central density about 3 times higher, but the axial ratios for a given mean radius are essentially identical with those found with an isothermal assumption. The axial ratios are between 1.55 and 1.7 for the prolate case, and between 1.6 and 1.75 for the oblate case, at average radii between 4′.5 and 10′. The average radius is defined as the square root of the product of the semimajor and semiminor radii.

IV. COMPARISON WITH OPTICAL RESULTS

The cluster A2256 has been comparatively well studied optically; the surface density of galaxies in the central regions of the cluster has been described (Bahcall 1975; Dressler 1978), the ellipticity of the galaxy distribution has been measured (Carter and Metcalfe 1980), and the redshifts of 15 galaxies have been determined (Bridle and Fomalont 1976; Faber and Dressler 1977), allowing an accurate distance determination (uncertainties in H_0 aside) and an estimate of the cluster velocity dispersion (Faber and Dressler 1977; Danese, De Zotti, and di Tullio 1980). We are thus able to compare the axial ratio and major-axis position angle of the galaxy distribution with the axial ratio and symmetry-axis position angle of the surfaces of constant total density derived from the X-ray data. In addition, the radially integrated cluster mass has been estimated from the optical data and may be compared with our result.

Carter and Metcalfe (1980) used a moment analysis to calculate the axial ratio and position angle of the cluster from a magnitude-limited sample ($M_F = 18.5$) of 369 galaxies obtained by Dressler (1976), covering a region 25′ on a side. This is the same sample of galaxies plotted in Figure 1. They obtained an axial ratio in the range of 2–3.3, and a position angle of 145° ± 6°, referring to a region of 7′.2 average radius. As before, the average radius is defined as the square root of the product of the major and minor radii. In the same region, assuming a 90° inclination angle, we obtain an axial ratio in the range of 1.56–1.69 for oblate or prolate geometries with isothermal or adiabatic temperature distributions. We note that for an inclination angle of 90°, the apparent projected axial ratio for spheroidal distributions with a constant axial ratio is identical with the true axial ratio. Therefore, the projected galaxy axial ratio may be directly compared with the 3-dimensional axial ratio we calculate. The position angle derived from the X-ray surface brightness data is 122° at 7′ average radius, and ranges between 112 and 125 degrees for average radii between 5′ and 16′.

The surface density distributions of galaxies have traditionally been fitted to the projected profile of an isothermal sphere, effectively neglecting the ellipticity of the distribution. Often the approximate King form (King 1972) $N(r) = N(0)/$

$[1 + (r/a)^2]$ is used for $r \lesssim 3a$, where the free parameters are the core radius a and the central density $N(0)$. This function (or its equivalent) was used by both Bahcall (1975) and Dressler (1978), who obtained core radii of 2′ and 4′.7, and central galaxy densities of 325 and 141 galaxies per cubic Mpc, respectively. These results were obtained from different samples (but overlapping to some degree), within a radius of 12′. The discrepancies between the fitted parameters reflects the difficulty of determining a core scale from a small number of objects. However, for a self-gravitating isothermal sphere, the velocity dispersion and core radius determine the central mass density (e.g., Zwicky 1957), and the cluster mass as a function of radius can be estimated by integrating the isothermal sphere density distribution or an analytic approximation (e.g., King 1972). The line-of-sight cluster velocity dispersion is uncertain because the number of measured reshifts is small; Danese, De Zotti, and di Tullio (1980) give a value of $1254(+323, -182)$ km s^{-1}. The quoted error does not include the possibly large systematic errors due to background contamination of the small sample.

The type of analysis just discussed neglects the velocity-dispersion anisotropy likely to be present in ellipsoidal clusters (Binney 1978; Richstone 1980). The technique used by Strimpel and Binney (1979) to analyze optical data from the Coma Cluster avoids this error, but the quantity of optical data presently available for A2256 does not allow its application. One could attempt a correction based on a knowledge of the mass distribution derived from the X-ray data, but the present errors in the velocity dispersion render this pointless.

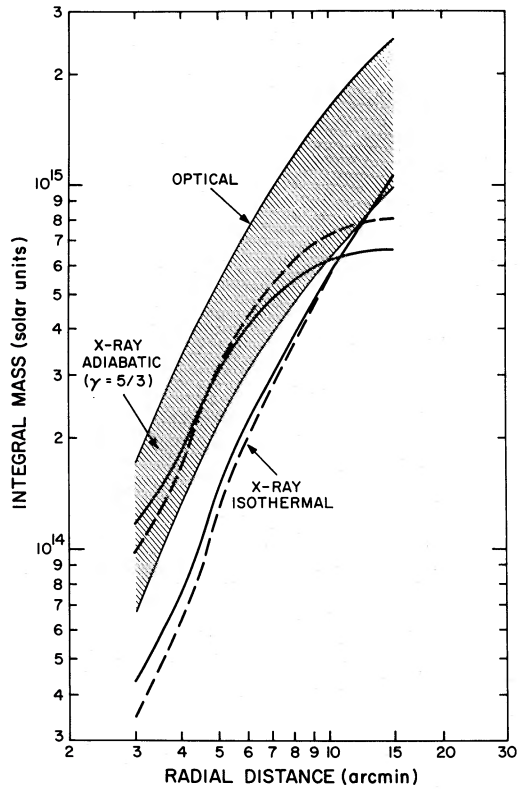

FIG. 10.—A plot of the radially integrated mass of A2256, based on optical work and the X-ray results presented here. The shaded region represents an optical mass estimate based on fits of the galaxy counts to the density distribution of the self-gravitating isothermal sphere (spherically symmetric) with a core radius of 4′.7 and line-of-sight velocity dispersions between 1000 and 1600 km s^{-1}. The X-ray mass estimates have been made assuming both oblate (*dashed line*) and prolate (*solid line*) geometries, and isothermal and adiabatic gas temperature distributions. For $H_0 = 50$ km s^{-1} Mpc^{-1}, the scale is 100 kpc arcmin^{-1}.

Figure 10 shows the radially integrated mass as a function of radius from the X-ray determined total density maps (isothermal or adiabatic, prolate or oblate) as well as the optically estimated mass for a core radius of 4′.7 and velocity dispersions between 1000 and 1600 km s^{-1}. The optically determined masses scale as the square of the velocity dispersion; the X-ray determined masses scale linearly with the gas temperature (eqs. [6] and [7]). The choice of a 2′ core radius is in poorer agreement with the X-ray results, with the mass lying a factor of 4 above the 4′.7 curve at a radius of 3′, and crossing below it at a radius of 9′. We note that Jones and Forman (1984) obtained a core radius of $4'.68 \pm 0'.21$ from the azimuthally averaged X-ray surface brightness data, consistent with Dressler's value.

One can see from Figure 10 that the X-ray and optical results are in reasonable agreement for a velocity dispersion on the low side of the range plotted. Although we may have underestimated the mass in the central few arc minutes of A2256 due to the 3′.5 FWHM resolution of the present X-ray map, the X-ray mass measurements are not completely dependent on the determination of a single (and apparently uncertain) core parameter as are the conventional optical mass estimates. In addition, the radially integrated mass obtained from the X-ray data is negligibly affected by the choice of an oblate or prolate geometry or the assumed inclination angle. In fact, if the ellipticity is neglected completely and the mass estimated by spherically symmetric techniques (e.g., Fabricant, Lecar, and Gorenstein 1980), one again arrives at the same radially integrated mass. The principal remaining error in the X-ray mass measurements is the lack of broad-band spatially resolved spectral data. The bandwidth of such future observatories as the Advanced X-Ray Astrophysics Facility (AXAF) will be fully adequate for this application.

V. SUMMARY AND CONCLUSIONS

We have described a new technique that allows the determination of the surfaces of constant total density within a cluster of galaxies from the X-ray surface brightness and spectral data. This method assumes that the cluster has a single axis of symmetry, and that the X-ray emitting gas is in hydrostatic equilibrium and is not supported by rotation. Given these assumptions, our remaining uncertainties concern the temperature distribution within the X-ray emitting gas and the unknown inclination angle between the line of sight and the cluster symmetry axis. We have estimated the effect of these uncertainties upon our results.

Consistent integral mass estimates for A2256 are obtained by using either the X-ray emitting gas or the galaxies as test particles to trace the gravitational potential. The precision of this comparison would be considerably improved if a larger sample of galaxy redshifts were available as well as a spatially resolved temperature profile of the gas. More detailed comparisons might allow us to decide, in addition, whether the oblate or prolate models are more applicable.

In one respect, the X-ray and optical results are somewhat discrepant; the X-ray estimated axial ratio of the total density distribution at an average radius of 7′ is 1.56–1.69, while the optically estimated axial ratio of galaxy positions at this radius is 2–3.3. This might be ascribable purely to measurement error,

most likely in the optical sample as the result of background contamination or statistical fluctuations, but the effect would be quite interesting if real, since it would imply a difference between the distribution of nonluminous and luminous matter. Binney (1977) has suggested that just such an effect might be produced by dynamical friction on the brighter galaxies, although other explanations involving a separation between the distributions of dissipationless dark matter and baryonic matter are possible. More detailed optical studies would be required to establish the reality of different axial ratios.

We wish to thank Margaret Geller and Myron Lecar for useful discussions, and Christine Jones and Daniel Schwartz for their comments on the manuscript.

APPENDIX

PROJECTIONS OF SPHEROIDS

Our purpose here is to derive equations (8)–(10). Similar results concerning projections can be found in Ruiz (1976) and Stark (1977).

The volume emissivity ϵ is assumed constant on concentric similar spheroidal contours with polar axis lying in the x-z plane and at inclination angle i to the z-axis. In terms of the coordinate system (x', y', z'), rotated in the x-z plane to make the z' axis lie along the polar axis, we have $\epsilon = G(\zeta)$, where

$$\zeta = \frac{x'^2 + y'^2}{B_e^2} + \frac{z'^2}{A_e^2} . \tag{A1}$$

Thus the ratio of polar to equatorial axes is A_e/B_e. In terms of (x, y, z),

$$\zeta = \frac{(x \cos i + z \sin i)^2}{B_e^2} + \frac{y^2}{B_e^2} + \frac{(z \cos i - x \sin i)^2}{A_e^2} . \tag{A2}$$

The projection onto the x-y plane is found from

$$I_i(x, y) = \int_{-\infty}^{\infty} G(\zeta) dz . \tag{A3}$$

Transforming the variable of integration from z to ζ, we obtain, after some considerable algebra,

$$I_i(x, y) = \frac{B_e}{R} F(\eta) \equiv \frac{B_e}{R} \int_{\eta}^{\infty} \frac{G(\zeta) d\zeta}{(\zeta - \eta)^{1/2}} , \tag{A4}$$

where

$$\eta \equiv \frac{x^2}{(RA_e)^2} + \frac{y^2}{B_e^2} \equiv \frac{x^2}{A^2} + \frac{y^2}{B^2} , \tag{A5}$$

$$R \equiv \left[\frac{B_e^2}{A_e^2} \cos^2 i + \sin^2 i \right]^{1/2} . \tag{A6}$$

Since $I_i(x, y)$ is a function of η alone, the observed isophotes are concentric ellipses with principal axes oriented along the y- and x-axes, with axial ratio equal to $(B/A) = R^{-1}(B_e/A_e)$; equation (10) then follows immediately. Substituting equation (10) in equation (A6), we can solve for R in terms of (B/A), which results in equation (9).

Setting $i = 90°$ in equation (A4), we obtain

$$I_{90}(x, y) = B_e F\left(\frac{x^2}{A_e^2} + \frac{y^2}{B_e^2} \right) = R I_i(Rx, y) , \tag{A7}$$

which is equation (8).

REFERENCES

Bahcall, N. 1975, *Ap. J.*, **198**, 249.
Binggeli, B. 1982, *Astr. Ap.*, **107**, 338.
Binney, J. 1977, *M.N.R.A.S.*, **181**, 735.
———. 1978, *M.N.R.A.S.*, **183**, 501.
Binney, J., and Strimpel, O. 1978, *M.N.R.A.S.*, **185**, 473.
Bridle, A., and Fomalont, E. 1976, *Astr. Ap.*, **52**, 107.
Carter, D., and Metcalfe, N. 1980, *M.N.R.A.S.*, **191**, 325.
Cavaliere, A. 1980, in *X-Ray Astronomy*, ed. R. Giacconi and G. Setti (Dordrecht: Reidel), p. 217.
Danese, L., De Zotti, G., and di Tullio, G. 1980, *Astr. Ap.*, **82**, 322.
Dressler, A. 1976, Ph.D. thesis, University of California, Santa Cruz.
———. 1978, *Ap. J.*, **226**, 55.
Faber, S., and Dressler, A. 1977, *A.J.*, **82**, 187.
Fabricant, D., Lecar, M., and Gorenstein, P. 1980, *Ap. J.*, **241**, 552.
Hirayama, Y., and Ikeuchi, S. 1978, *Progr. Theor. Phys.*, **60**, 1337.
Jones, C., and Forman, W. 1984, *Ap. J.*, **276**, 38.
King, I. 1972, *Ap. J. (Letters)*, **174**, L123.
Merritt, D. 1983, *Ap. J.*, **264**, 24.
Mitchell, R., Dickens, R., Bell Burnell, S., and Culhane, J. 1979, *M.N.R.A.S.*, **189**, 329.

Mushotzky, R., Serlemitsos, P., Smith, B., Boldt, E., and Holt, S. 1978, *Ap. J.*, **225**, 21.
Richstone, D. 1980, *Ap. J.*, **238**, 103.
Ruiz, M. 1976, *Ap. J.*, **207**, 382.
Rybicki, G. 1984, in preparation.
Stark, A. 1977, *Ap. J.*, **213**, 368.
Strimpel, O., and Binney, J. 1979, *M.N.R.A.S.*, **188**, 883.
Zwicky, F. 1957, *Morphological Astronomy* (Berlin: Springer).

DANIEL G. FABRICANT: Harvard-Smithsonian Center for Astrophysics, 60 Garden Street, Cambridge, MA 02138

GEORGE B. RYBICKI: Harvard-Smithsonian Center for Astrophysics, 60 Garden Street, Cambridge, MA 02138

PAUL GORENSTEIN: Harvard-Smithsonian Center for Astrophysics, 60 Garden Street, Cambridge, MA 02138